

A Spitzer/IRAC Census of the Asymptotic Giant Branch Populations in Local Group Dwarfs. I. WLM

Dale C. Jackson, Evan D. Skillman, Robert D. Gehrzi, Elisha Polomski, and Charles E. Woodward

Astronomy Department, University of Minnesota, 116 Church St. S.E., Minneapolis, MN 55419

`djackson@astro.umn.edu, skillman@astro.umn.edu, gehrzi@astro.umn.edu,`
`elwood@astro.umn.edu, chelsea@astro.umn.edu`

ABSTRACT

We present *Spitzer*/IRAC observations at 3.6 and 4.5 μm along with optical data from the Local Group Galaxies Survey to investigate the evolved stellar population of the Local Group dwarf irregular galaxy WLM. These observations provide a nearly complete census of the asymptotic giant branch (AGB) stars. We find 39% of the infrared-detected AGB stars are not detected in the optical data, even though our 50% completeness limit is three magnitudes fainter than the red giant branch tip. An additional 4% of the infrared-detected AGBs are misidentified in the optical, presumably due to reddening by circumstellar dust. We also compare our results with those of a narrow-band optical carbon star survey of WLM, and find the latter study sensitive to only 18% of the total AGB population. We detect objects with infrared fluxes consistent with them being mass-losing AGB stars, and derive a present day total mass-loss rate from the AGB stars of $\dot{M} = 0.7\text{--}2.4 \times 10^{-3} M_{\odot} \text{ yr}^{-1}$. The distribution of mass-loss rates and bolometric luminosities of AGBs and red supergiants are very similar to those in the LMC and SMC and the empirical maximum mass-loss rate observed in the LMC and SMC is in excellent agreement with our WLM data.

Subject headings: stars: AGB - stars: carbon - stars: mass loss - galaxies : dwarf - galaxies : irregular - galaxies : Local Group - galaxies : individual(WLM)

1. Introduction

Dwarf galaxies are the most common type of galaxies in the universe. Understanding their formation and evolution is an important step in understanding the evolution of all

galaxies since they are likely the building blocks of more massive systems like the Milky Way. Because the basic properties of dwarf galaxies (luminosity, stellar and gaseous mass, star formation rate (SFR), and metallicity) are very different from those of massive galaxies, detailed studies of the former objects provide us with an important tool to understand better how the astrophysics of star formation and galaxy evolution depend on these characteristics. The dwarf galaxies of the Local Group, in particular, provide a wealth of information about their evolution; unlike more distant objects, we are able to resolve them into individual stars to study the characteristics of their stellar populations and to create detailed star formation histories (SFHs).

The Local Group dwarf irregular (dI) galaxy WLM, first discovered by Wolf (1909) and independently rediscovered by Lundmark and Melotte (Melotte 1926), has been the subject of many investigations over the past two decades (cf., van den Bergh 2000). Huchtmeier et al. (1981) and Huchtmeier & Richter (1986) first addressed the H I properties of the galaxy, finding it to be gas-rich, in keeping with its dI morphology. Jackson et al. (2004) were the first to resolve the galaxy in H I, and found a double-peaked flux distribution. Because WLM is relatively nearby ($m - M = 24.88$; Dolphin 2000), the stellar population is easily resolved, enabling high quality optical photometry. Dolphin (2000) and Rejkuba et al. (2000) find WLM’s SFH suggests the bulk of the stars formed over 9 Gyr ago. This episode of star formation was followed by a gradual decrease in the star formation rate until the most recent event that began between 1 and 2.5 Gyr ago and continues today (Hodge & Miller 1995; Skillman et al. 1989; Hunter et al. 1993; Lee et al. 2005). Jackson et al. (2006) studied the emission from hot dust and polycyclic aromatic hydrocarbons (PAHs) and found only very low surface brightness emission coincident with the highest surface brightness H II regions, as is expected from a galaxy with relatively low metallicity ($12 + \log(O/H) = 7.83$; Lee et al. 2005) and current star formation rate ($0.003 M_{\odot} \text{ yr}^{-1}$; Mateo 1998).

The evolved stellar population of WLM was examined by Cook et al. (1986) and Battinelli & Demers (2004), who both found an extremely high carbon star to M-type asymptotic giant branch (AGB) star ratio in accordance with its low metallicity (Iben & Renzini 1983). Other studies using narrow-band filters centered on the CN and TiO absorption features have enabled the study of AGBs in a limited sample of Local Group galaxies (Cook et al. 1986; Nowotny et al. 2001; Battinelli & Demers 2005). Because optical studies can suffer significantly from extinction effects (due to both the host galaxy interstellar medium (ISM) and the winds of individual stars), many AGB studies have been performed in the infrared (IR)(e.g., Boyer et al. 2006; Zijlstra et al. 1996; Wood 1998; van Loon et al. 1999, 2005). The majority of this effort has been limited to the Galaxy and the Magellanic Clouds because a combination of poor angular resolution and observational sensitivity made similar investigations in more distant systems impossible. However, near-IR studies of other Local Group galaxies (par-

ticularly dwarf spheroidals) recently have been conducted with the large-aperture ground based telescopes (Babusiaux et al. 2005; Cioni & Habing 2005; Davidge 2005; Kang et al. 2005; Sohn et al. 2006).

In this paper we present *Spitzer Space Telescope* imaging of WLM at 3.6 and 4.5 μm . These observations provide us with the first high-resolution ($0.9'' \text{ pixel}^{-1} = 4 \text{ pc pixel}^{-1}$) high-sensitivity thermal-IR images of this galaxy, enabling us to investigate the evolved stellar population in WLM. Section 2 describes the observations and reduction of the *Spitzer* data as well as previously unpublished data from the Local Group Survey (Massey et al. 2006). In §3 we discuss the morphology of WLM as a function of wavelength. We address both the optical and IR photometry in §4 and discuss the AGB and carbon star population. We derive mass-loss rates and wind optical depths in §5.3. In §5.4 we investigate the contributions from various stellar types to the near-IR luminosity of WLM.

2. Observations and Data Reduction

2.1. Infrared and Optical Data and Photometry

Spitzer Space Telescope (Werner et al. 2004) data of WLM were obtained with the Infrared Array Camera (IRAC; Fazio et al. 2004) in two separate AORs on 2003 December 12 UT and 2005 December 23 UT (AORKEYs: r5051136 and r15892480, respectively). Both AORs of WLM were done as part of a larger guaranteed time observing program (PID: 128, PI: R.D. Gehrzi).

IRAC provides simultaneous imaging at 3.6, 4.5, 5.8, and 8.0 μm ; however, the field of view at 3.6 and 5.8 μm are offset from that at 4.5 and 8.0 μm . To map WLM most efficiently a 1×4 mosaic was created, leaving a coverage area in all four IRAC bands of approximately $4' \times 12'$ centered on $\alpha=00:02:00$, $\delta=-15:28:30$ (Figure 1). Throughout this paper all discussions refer to this region only. A total exposure time of 500 seconds per pointing was used for all bands.

The IRAC data (pipeline version 13.2.0) were reduced using the MOPEX¹ reduction package, version 2006 March 1. The overlap routine was used to match the backgrounds of individual frames to create a smooth background in the final mosaic. Outlier detection, image interpolation, and image co-addition were done with the mosaic program which also created the final mosaics. The 8.0 μm data taken in 2003 were strongly affected by persistent

¹MOPEX is available from the Spitzer Science Center at <http://ssc.spitzer.caltech.edu/postbcd/>

images resulting from bright sources imaged in the program immediately before our AORs were executed. Subtracting a median-combined image of all of the dithered frames from each frame proved very effective at removing these artifacts.

Point source photometry was done with the DAOPHOT II photometry package (Stetson 1987). For the relative photometric errors, we adopt the formal errors produced by DAOPHOT. IRAC has an estimated absolute calibration accuracy of 3% (Reach et al. 2005). Due to the high sensitivity of these observations, a significant number of background galaxies are detected. A sharpness clip, which identifies detections that are best fit by a point spread function (PSF) much broader or narrower than our template PSF, was applied to all bands to produce our final photometry list, which proved effective at removing extended objects.

Broadband U, V, and I images of WLM were obtained from the Local Group Galaxies Survey² (LGGS, Massey et al. 2006). The ground-based optical imaging from the LGGS complements the *Spitzer*/IRAC imaging nicely because they have similar angular resolutions. The U image was used only to investigate the change in galaxy morphology with wavelength and no photometry was performed on this image. Because our use of the V and I data was solely to identify stellar types via color magnitude diagrams to then cross-identify these sources in the near-IR, precise absolute photometry was not required. Consequently, ‘stacked’ images that have relative photometric errors of $\sim 10\%$ were used rather than the ‘photometric’ images since image processing, including co-addition and astrometric calibration, were already performed on the former.

No photometric calibrations have yet been released for the V and I data. Consequently, to calibrate the magnitude offsets between instrumental and true magnitudes, we compared our photometry to that of the photometrically calibrated Hubble Space Telescope (HST) Local Group Stellar Photometry Archive (Holtzman, Afonso, & Dolphin 2006). These data are publicly available, and one HST/WFPC2 pointing ($< 6 \text{ arcmin}^2$) is entirely contained in our IRAC coverage. The Massey et al. (2006) data cover a $36' \times 36'$ field of view, including our entire *Spitzer* coverage area. The magnitude offsets and color terms for sources with centroids matching those in the HST photometry were calculated using least squares fitting. The appropriate offsets were then applied to all the detected sources in the V and I photometry. The optical and IR photometric catalogs were combined by matching point sources that have the same centroids within a tolerance of $\pm 1''$. Throughout this paper all magnitudes are stated with respect to α Lyr (Vega).

²LGGS data are publicly available at <http://www.lowell.edu/~massey/lgsurvey/>

2.2. Foreground Star Contamination

In §4 we examine the properties of the evolved stellar population in WLM. Because these objects can have similar apparent magnitudes and colors to Galactic late-type dwarfs, it is important to determine the extent to which our data will be affected by contamination by Galactic foreground stars. We estimated the number of foreground stars in our IR data using the Milky Way stellar population synthesis model of Robin et al. (2003). We chose a field one square degree in size centered on the Galactic coordinates of WLM to provide robust statistics. This model provides magnitudes for modeled stars in L band, whose central wavelength is close to that of the $3.6\ \mu\text{m}$ IRAC band.

From this model we expect only 9 foreground stars in the area from which our IR CMD was constructed with $-13 < M_{3.6} < -5$. These are all expected to have $[3.6]-[4.5]$ colors very near zero.

3. Optical and IR Galaxy Morphology

WLM is a highly-inclined ($i = 69^\circ$; Ables & Ables 1977; Jackson et al. 2004) disk galaxy, elongated almost exactly north-south. Its overall appearance varies considerably from optical to IR wavelengths. Figure 2 shows the U (a), I (b), and continuum-subtracted $\text{H}\alpha$ (c) images of WLM. In the U image there is a prominent feature arcing to the north-west. The rest of the emission consists of four associations in the central and southern galaxy that are currently undergoing star formation, as is evident from the $\text{H}\alpha$ emission. In the I image we see the galaxy morphology change from that of a well defined arc and distinct star forming regions to a much smoother stellar distribution. The $\text{H}\alpha$ emission is confined to the central and southern parts of the galaxy, with no detected emission in the northern arc. There is a large loop of $\text{H}\alpha$ emission to the southwest, directly across from which (to the northeast) is a large area of very low surface brightness $\text{H}\alpha$ emission. This low surface brightness feature is coincident with the central region of WLM that is H I deficient (northeast of the two H I peaks in Jackson et al. 2004). We take this as further evidence of a partial blowout of the ISM by the massive young stellar population.

The IRAC images of WLM are shown in Figure 3. The appearance of the galaxy retains the smooth stellar distribution observed in the I image with the addition of a large population of very luminous objects throughout the galaxy (AGBs or red supergiants [RSGs]). Jackson et al. (2006) detected extremely faint diffuse $8.0\ \mu\text{m}$ emission in WLM, coincident with the high surface brightness H II regions HM7 and HM9 (Hodge & Miller 1995). In §4 we discuss how the distribution of AGB stars compares with that of the other stellar

populations.

4. Comparative Optical and IR Photometry

As described in §2 we created a master photometry list, which includes detections in V, I, and all four IRAC bands. The optical properties of the stellar populations have been discussed by other authors (Hodge et al. 1999; Rejkuba et al. 2000; Minniti & Zijlstra 1997) and we will not address them here. The optical color-magnitude diagram (CMD), shown in Figure 4 is segregated into sections consisting of blue objects (a), AGB stars (b), RSGs (c), and red giants (d), enabling us to ascertain where these stellar types lie in the IR CMD (described below), as the infrared colors of the objects detected with IRAC are much less sensitive to effective temperature than those in the optical. The loci of stellar types were conservatively chosen, with gaps between them, so that stars will not be misidentified solely due to photometric errors (though as we discuss below, reddening from dust absorption can certainly lead to such misidentification).

The $3.6 \mu\text{m}$ absolute magnitude versus $[3.6] - [4.5]$ IR CMD is shown in Figure 5. The basic structure of the IR CMD is a vertical distribution of stars with $[3.6] - [4.5]$ very near zero. This vertical feature contains all objects where both the 3.6 and $4.5 \mu\text{m}$ bands sample the Rayleigh-Jeans tail of the Planck function. Any unreddened object with spectral type earlier than G0 will have $[3.6] - [4.5]$ very close to zero, while K0–M5 stars become progressively *bluer* to a color of -0.25 due to CO absorption at $4.6 \mu\text{m}$ (Jones et al. 2005).

A vector showing 10 visual magnitudes of extinction (Indebetouw et al. 2005; Rieke & Lebofsky 1985) as well as the AGB limit are included in the IR CMD. While the reddening vector takes into account the wavelength dependent extinction from dust, it does not include the circumstellar emission, which can be significant at longer wavelengths. The AGB limit was determined by assuming a bolometric correction at $3.6 \mu\text{m}$ of +3 magnitudes for an M5 star, +2 magnitudes for a G0 star and $M_{bol} = -7.1$ (Wood et al. 1983), and is depicted in Figure 5 as a line connecting the AGB limit for these two stellar types. Above the plotted AGB limit we detect two optically classified RSGs and one optically classified AGB star. The object optically classified as an AGB star lies just within the blue boundary of region (b) and could easily be a slightly reddened RSG. There are also six objects brighter than, but redward of the AGB limit that are optically classified as AGB stars. Based on their positions in the optical CMD, the brightest three of these six objects are likely reddened RSGs, while the fainter three are consistent with mass-losing AGB stars (see §5.3 for a description of the effect of mass-loss on the $[3.6] - [4.5]$ color).

There is considerable overlap in the lower part of the IR CMD between stellar types. However, the luminosity of the red giant branch tip (TRGB) does enable us to separate red giants from the other stellar types. Figure 6 shows the $3.6\text{ }\mu\text{m}$ luminosity function for all objects detected at both 3.6 and $4.5\text{ }\mu\text{m}$. Based on the abrupt drop in the $3.6\text{ }\mu\text{m}$ luminosity function, we adopt a $3.6\text{ }\mu\text{m}$ absolute magnitude of the TRGB to be -6.6 . This value for the TRGB is slightly brighter than the value adopted by van Loon et al. (2005) for the LMC ($L' = -6.4$), though given the uncertainty in the distance modulus to WLM (± 0.08 magnitudes) and the bin size of our luminosity function (0.25 magnitudes) these values agree reasonably well. For the objects detected at both 3.6 and $4.5\text{ }\mu\text{m}$, 79% of the total $3.6\text{ }\mu\text{m}$ flux of 46.5 mJy is from stars brighter than the TRGB, which are predominantly AGB stars.

The right panel of Figure 5 shows the IR CMD of objects detected in V, I, and at 3.6 and $4.5\text{ }\mu\text{m}$, separated according to their optically selected stellar type. The optically detected AGB stars have typical IR colors of $-0.25 < [3.6] - [4.5] < 0.25$, with the exception of a few luminous red sources. The RSGs have a similar distribution, although no RSGs with red IR colors are detected, as any reddening would cause a RSG to be misidentified as an AGB star in the optical. Nearly all of the blue objects detected in the optical and IR are found between $-8 < M_{3.6} < -5$ and $-0.3 < [3.6] - [4.5] < 0.5$. We also detect a few IR luminous ($M_{3.6} \sim -9$) unresolved H II regions that are coincident with strong H α emission. The optically identified red giants are peaked at $M_{3.6} = -6$, due to our completeness limit (see Figure 5), and have a large range in color $-0.5 < [3.6] - [4.5] < 1$. As we will discuss in §5.1, there are also a large number of optically classified red giants that lie above the TRGB in the IR, which are consistent with the colors of reddened AGB stars.

Figure 7 is the CMD for all sources detected at both 3.6 and $8.0\text{ }\mu\text{m}$. Because of both reduced sensitivity (1- σ point source sensitivity of $4.4\text{ }\mu\text{Jy}$) and fainter emission from stellar photospheres, we detect significantly fewer sources at $8.0\text{ }\mu\text{m}$ than in the shorter wavelength bands. However, the longer wavelength baseline can be useful for separating sources enshrouded in circumstellar material (such as carbon stars) due to the emission from dust at $8.0\text{ }\mu\text{m}$. In this CMD, apparently two separate populations are present; a narrow distribution with $-12 < M_{3.6} < -9$ and $[3.6] - [8.0] \sim 0$ that are indicative of the brightest AGBs and RSGs that also have $[3.6] - [4.5] \sim 0$, consistent with normal AGBs or RSGs not undergoing mass-loss, and another, much broader, distribution with $-12 < M_{3.6} < -9$ and $1 < [3.6] - [8.0] < 4$ that are likely AGBs losing significant mass.

In Figure 8 we show the Right Ascension and Declination of point sources based on their optical/IR classification. The optically classified blue objects are strongly concentrated in the regions of active star formation and the northern arc, while the AGB stars are much more smoothly distributed. The red giants are also smoothly distributed over the face of WLM,

though this plot shows the effect that crowding from both blue objects that are very bright in the optical, and red giants, whose stellar density increases toward the center of WLM, have on the completeness of fainter sources such as red giants (e.g., there are ‘holes’ in the detected red giant distribution toward the center of WLM, particularly at the locations of recent star formation).

Table 2 lists many of the detection statistics for our optical and infrared photometry. For the region in WLM with coverage in all four IRAC bands we detect 2855, 2019, 300, and 122 point sources at 3.6, 4.5, 5.8, and 8.0 μm , respectively. For the same region we detect 4989 objects in our matched V and I photometry. We find 46 objects (38% of all 8.0 μm detections) that are detected in all four IRAC bands with no optical counterpart. Of these, 5 have 3.6 and 4.5 μm fluxes consistent with RSG stars (i.e., they are above the AGB limit), while the remaining 41 stars could be either RSGs or AGBs.

In the IR CMD we find a population of bright, red objects to the right of the main vertical distribution of stars ranging from $M_{3.6} = -10$ and $[3.6] - [4.5] = 0.3$ to $M_{3.6} = -7.5$ and $M_{3.6} - [4.5] = 1.2$. Eleven of the 31 objects are detected in the optical, with seven being AGB stars, two unresolved H II regions coincident with strong H α emission, and two objects that are probably foreground giants. It is likely that many of the objects not detected in the optical are dust enshrouded AGB stars, since only the brightest and bluest of these objects are detected optically and the majority of these are optically classified as AGBs (see the discussion in §5.3).

5. The AGB Stars

Due to the micro-Jy point source sensitivity of IRAC with our integration time, we should be able to detect the entire population of the AGB stars in WLM, excluding only those objects that were not detected due to crowding. However, uniquely determining the true stellar types of the detected objects can be challenging, as the spectral energy distributions (SEDs) of these stellar types, with the exception of unresolved H II regions, are indistinguishable from one another.

Figure 9 shows the IRAC SEDs for the all of the AGB stars, RSGs, and blue objects detected in all four IRAC bands and the LGGS V and I images. This plot shows the similarity between the infrared fluxes of AGBs and RSGs. Although it is challenging to distinguish between AGB stars and RSGs using IRAC data alone, the combination of optical and near-IR data provide a powerful method of detecting candidate AGB stars in galaxies past the immediate vicinity of the Milky Way, since RSGs are generally easily identified in optical

CMDs.

5.1. Optical Completeness

One of the goals of our study is to determine the fraction of AGB stars seen in the IR that were not detected in the optical due to extinction by circumstellar material. To estimate this fraction, we make the approximation that all objects above the TRGB in the IR CMD are AGB stars. While there is contamination above the TRGB from RSGs and blue objects, the number of these objects detected in the optical contribute $\lesssim 10\%$ of the population above the TRGB in the IR.

Of the 691 stars brighter than the TRGB in the IR, 39% are not detected in V and I. There are also 29 objects brighter than the TRGB in the IR CMD, but lie within region (d) of the optical CMD (the region surrounding red giants) at positions such that they could have been reddened from above the TRGB via the reddening vector shown in Figure 4. We find it likely that these 29 objects are AGB stars whose optical fluxes suffer extinction by circumstellar material.

It is important to consider the effects of photometric scatter as well as errors due to blending, crowding, and even on our adopted value of the TRGB on these completeness statistics. By shifting our adopted value of the TRGB ($M_{3.6} = -6.6$) up or down by 0.5 magnitudes, the fraction of optically detected AGB stars changes by only a few percent. This is not unexpected though. Most of the AGB stars detected in the IR but not in the optical are considerably brighter than the TRGB, because the mass-loss phase that hides AGB stars in the optical typically takes place at luminosities above the TRGB. Therefore, even if a number of sources were scattered from above the TRGB to below, or visa versa, the fraction of optically detected AGB stars would change very little. This problem is more significant, however, for the number of AGB stars misidentified as red giants because of the large number of optically identified red giants just below the TRGB. If we shift the adopted value of the TRGB to be 0.5 magnitudes fainter, the fraction of objects we would classify as AGB stars in the IR, but optically identified as red giants would increase from 4% to 8%. Because the average $3.6\ \mu\text{m}$ photometric error at the TRGB is only 0.1 magnitudes, it is unlikely that the fraction of AGBs misidentified as sub-TRGB red giants in the optical has been effected by more than 1–2%.

Further, in the most crowded region of our IRAC images, we detect only 0.04 stars at 3.6 and $4.5\ \mu\text{m}$ per area the size of the 3.6 micron FWHM disk. Consequently, we do not anticipate crowding or blending effects to contribute significantly to the overall photometric

errors of our sources, although it certainly may affect some of them.

In summary, we find that 43% of the AGB stars in WLM are enshrouded with enough material to make them either undetectable or misidentified in the optical CMD, even though in V and I the 50% completeness level is nearly three magnitudes below the TRGB. This number of optically-undetected AGB stars is consistent with other studies (e.g., van Loon et al. 1997; Wood 1998; van Loon et al. 2006a) that find a significant fraction of the AGB population (in particular the carbon stars) in an obscured state. Future investigations of other galaxies from this same observing program will allow us to determine the dependence of this fraction on the metallicity of the host system. It should again be noted that we are ignoring the faint end of the AGB distribution, i.e., any AGBs fainter than the TRGB.

The completeness fraction discussed above has important implications for the intermediate age SFH one would derive from galaxies like WLM. Programs that derive SFHs from optical CMDs (e.g., Dolphin 2002) would tend to over-predict the number of detected AGB stars, based on the number of main sequence stars, since many of the AGBs have been reddened beyond the optical detection limit. Consequently, it is important to apply either corrections to the number counts in this part of the CMD, or weighting functions to give more confidence to the number of detected intermediate age main sequence stars, rather than the AGB stars. As shown here, at least for WLM, there must be allowance for a factor of 2 in the disparity between the number of main sequence and AGB stars used to measure the intermediate age star formation rate. If such disparities are not accounted for, one will underestimate the true star formation rate over the past few Gyr.

5.2. The Carbon Stars

Battinelli & Demers (2004) studied the carbon stars in WLM using narrow-band optical filters centered on the CN and TiO absorption features. At 3.6 and 4.5 μm we detect nearly all of the 111 carbon stars detected by Battinelli & Demers (2004) that are within our coverage area (our entire IRAC coverage area is within the Battinelli & Demers (2004) field). The remaining 11 objects were not detected in the IRAC data due to crowding, but were detected in the Massey et al. (2006) optical data. In Figure 10 we plot our IRAC photometry of the carbon stars identified by Battinelli & Demers (2004). The carbon stars span a relatively wide range of absolute 3.6 μm magnitudes (from 15.75 to 18) and [3.6]–[4.5] colors (from –0.3 to 0.6).

The Battinelli & Demers (2004) photometry is valuable in its ability to distinguish between carbon-rich and oxygen-rich AGB stars. However, the 111 carbon stars and 12 M-type

AGBs detected in the Battinelli & Demers (2004) study comprise only \sim 18% of the AGB stars detected in our IRAC data. This is surprising, given that the broadband portion of their data are shown to be complete 1 magnitude below the TRGB, and other comparable studies (Albert et al. 2000; Battinelli et al. 2003) have estimated completeness near 90%. There are two explanations that could lead to this disparity. Either Battinelli & Demers (2004) have overestimated their completeness limit, or in this work we have underestimated the contamination above the TRGB from stellar types other than AGB stars. We know from comparison with the optical data (§4) that at least 10% of the stars above the TRGB in the IR are not AGB stars. However, for contamination of other stellar types to be solely responsible for the difference between these two studies, this fraction would need to be 90%, i.e., there would need to be vastly more optically undetected RSGs, foreground stars, or other objects besides AGBs. This seems unlikely, considering the relative number of optically detected RSGs and AGBs shown in Figure 4, and the very small number of expected foreground stars.

It is clear from Figure 10 that the carbon stars detected in the narrow-band study have relatively blue [3.6]–[4.5] colors, with only very bright carbon stars being detected with even moderately red colors. We also detect a number of objects with $M_{3.6}$ between -7 (i.e., the faintest carbon stars detected by the narrow-band study) and the TRGB. The red AGBs that were not detected by Battinelli & Demers (2004) can be explained by circumstellar material reddening them beyond their detection limits. However, the faint AGBs with blue [3.6]–[4.5] colors that were not detected are somewhat more perplexing. Because AGB stars cannot become carbon stars until after thermal pulsing begins (when they are somewhat brighter than the TRGB), we would expect the region between the TRGB and the faintest carbon stars to be filled with oxygen-rich AGBs. If the AGBs we detect between the TRGB and the faintest carbon stars are oxygen-rich AGBs, they would not be expected to have significant mass-loss rates, and consequently should be detectable in the optical. One possible explanation for these non-detections is that a brightness limit in the Battinelli & Demers (2004) data was created by the requirement that the combined broad- and narrow-band photometric errors be small, which would tend to remove faint, low signal-to-noise detections. There are also a number of objects with $M_{3.6}$ between -7 and the TRGB that have red [3.6]–[4.5] colors. Because AGBs just above the TRGB are not expected to have large mass-loss rates, the red colors of many of these objects are likely due to point source blending or photometric scatter, rather than objects with significant mass-loss.

It is instructive to compare these completeness results with the deep near-IR imaging of NGC 6822 by Cioni & Habing (2005). They detect a total of 6195 AGB stars in their J and K_S imaging; of which 4684 are oxygen-rich and 1511 carbon-rich for a carbon star to M-type AGB (C/M) ratio of 0.32. When including I , J , and K_S they find 2161 oxygen-rich

and 500 carbon-rich AGBs for a C/M ratio of 0.23. This is in comparison with the \sim 1800 AGB stars (904 carbon stars and C/M = 1.0 ± 0.2) detected in the narrow-band optical study of NGC 6822 by Letarte et al. (2002). The fraction of AGBs (both C and M-type) detected in the optical study of Letarte et al. (2002) is somewhat artificially inflated though, since the field of view of their study was larger than that in the near-IR study of Cioni & Habing (2005). It is intriguing to note that while the Letarte et al. (2002) optical study detected significantly fewer AGBs total, the C/M ratio they found was higher. This is contrary to what we would predict, given the assumption that carbon stars should be more difficult to detect in the optical.

It is not clear what the implications of this incompleteness are for studies of the effect of host galaxy metallicity on the C/M ratio. Because AGB winds composed of oxygen-rich compounds are less efficient at absorbing visible photons than those that are carbon-rich (Wallerstein & Knapp 1998), optical studies should be more adept at detecting M-type rather than carbon-rich AGBs. Consequently, the incompleteness of the Battinelli & Demers (2004) study may mean the C/M ratio may be even higher than the value they derive, C/M = 12.4, with a large uncertainty because of the difficulty in distinguishing between M-type AGBs and foreground Galactic dwarfs. On the other hand, there are a number of AGBs not detected in the Battinelli & Demers (2004) study between the TRGB and the faintest carbon stars, which is where we would expect oxygen-rich AGBs to reside. This leads us to conclude that many more M-type AGBs were not detected, lowering the assumed C/M ratio. Shorter-wavelength near-IR images of WLM (such as in the J, H, and K_S bands) would be extremely useful in this case, since they could be used to distinguish between oxygen- and carbon-rich AGB stars and are also less effected by extinction from circumstellar material than the optical studies.

5.3. Mass-Loss Rates

Using the dust radiative transfer models from Groenewegen (2006), we can estimate wind optical depths (τ) and mass-loss rates (MLRs) for the AGB stars in our IRAC data. Groenewegen (2006) presents a number of models including carbon- and oxygen-rich AGBs and post-AGBs with varying effective temperatures and wind compositions (including amorphous carbon (AMC) and silicon carbide (SiC) for the carbon stars and aluminum oxide (AlOx) and silicates (Si) for oxygen-rich AGBs). In Figure 11 we show representative models, displayed as tracks indicating where an AGB in WLM would move with increasing τ or MLR of a given composition.

For the carbon-rich AGBs, these models show very little difference in the position on

the CMD between winds composed of 100% AMC or 85% AMC and 15% SiC. At large τ there is also very little difference between effective temperatures ranging from 2650 K to 3600 K. At small τ ($\tau_{11.75 \mu\text{m}} \sim 10^{-4}$), cooler effective temperatures correspond to the same $M_{3.6}$ magnitude but redder [3.6]–[4.5] colors. If the main vertical distribution in our IR CMD is composed of carbon stars with negligible MLRs, the majority have effective temperatures slightly cooler than 3600 K. It is interesting to note that while some of the spread in color of the vertical distribution is certainly due to increasing photometric scatter with increasing $M_{3.6}$ magnitude, this spread is also consistent with the range of modeled effective temperatures.

For the oxygen-rich AGBs at a given effective temperature, varying the composition of the wind from 100% AlOx, to 60% Si and 40% AlOx, and to 100% Si yield tracks roughly the same shape. However, increasing the Si fraction shifts the tracks redward. Changing the spectral type for a given wind composition from M0 to M6 to M10 produces brighter $M_{3.6}$ magnitudes and redder [3.6]–[4.5] colors.

Because of the similarities between the tracks of oxygen- and carbon-rich AGBs, we cannot distinguish between them in our CMD. However, we can still investigate the MLRs of AGB stars by comparing the distribution of our sources to the various models. The [3.6]–[4.5] color of AGB stars corresponds to a unique τ , which in turn corresponds to a MLR, scaled by the square root of the stellar luminosity and by the inverse of the dust-to-gas ratio (ψ) for a given stellar/wind composition, as prescribed by Groenewegen (2006). We calculated the total MLRs by binning the AGBs according to the modeled optical depths and applying the appropriately scaled MLR, given the stellar color and luminosity. Dolphin (2000) estimates the metallicity of WLM 1-2.5 Gyr ago (an appropriate timescale for the formation of the current AGB population) to be $[\text{Fe}/\text{H}] = -1.13$, while the current metallicity of WLM, as measured by both the nebular oxygen abundance (Lee et al. 2006) and blue supergiants (Bresolin et al. 2006) is $[\text{O}/\text{H}] = -0.8$. These upper and lower limits give us a reasonable range of values for the expected metallicities of the AGB population, and also allow us to estimate an uncertainty in the calculated MLRs. Assuming the dust-to-gas ratio scales as $\psi = \psi_{\odot} 10^{-[\text{Fe}/\text{H}]}$ and $\psi_{\odot} = 0.005$ (van Loon et al. 2005), we adopt $\psi_{\text{WLM}} = 3.7\text{--}7.9 \times 10^{-4}$.

If the entire AGB population is composed of carbon-rich AGBs with $T_{\text{eff}} = 3600$ K and wind composition of 85% AMC and 15% SiC we derive a total MLR of $\dot{M} = 1.1\text{--}2.4 \times 10^{-3} M_{\odot} \text{ yr}^{-1}$. If instead we assume a population with the same properties except $T_{\text{eff}} = 2650$ K, we find a similar total MLR of $\dot{M} = 0.9\text{--}1.9 \times 10^{-3} M_{\odot} \text{ yr}^{-1}$. In both of these cases we are not including the contribution from sources bluer than the model colors; however, these objects contribute a negligible amount to the total MLR. Ninety percent of the total MLR from both models are from sources with $[\text{3.6}]\text{--}[\text{4.5}] > 0.5$, and over 50% of the mass-loss

is from sources with $[3.6]-[4.5] > 1.0$. The total MLRs are a factor of 3.3 higher if the population is composed of oxygen-rich AGBs with 60% Silicate and 40% AlOx winds, and a factor of 2.9 higher for oxygen-rich AGBs with 100% silicate winds.

We are particularly interested in the sources redward of the main stellar distribution (shown in the box in the right panel of Figure 11). These sources are well modeled by both oxygen-rich AGBs with $\tau_{11.75 \mu\text{m}} = 3.0$ and carbon-rich AGBs with $\tau_{11.75 \mu\text{m}} = 0.54$. The only models ruled out by these data are an entire population of oxygen-rich AGBs with a wind composed of 100% aluminum oxide (at any T_{eff}), since even at the largest modeled τ ($\tau_{11.75 \mu\text{m}} = 18.5$) these objects do not become red enough to reproduce the observed distribution. It is appropriate to calculate a more conservative MLR, based solely on these objects, since many sources that are consistent with having moderate MLRs may have artificially red colors due to photometric scatter and/or point source blending. The MLRs calculated using only these objects are $0.8-1.6 \times 10^{-3} M_{\odot} \text{ yr}^{-1}$ for carbon stars with $T_{\text{eff}} = 3600 \text{ K}$ and $0.7-1.4 \times 10^{-3} M_{\odot} \text{ yr}^{-1}$ for $T_{\text{eff}} = 2600 \text{ K}$. This box was chosen somewhat arbitrarily, however, moving the blue boundary of the box to include AGBs with moderate $[3.6]-[4.5]$ colors changes the total MLR by less than 10%, since the overall mass-loss is dominated by the handful of very red sources.

Because the mass-loss rates we derive are so strongly dependent on the few reddest sources in this galaxy, it is imperative that we be confident that these sources are real and have not been created by photometric errors or the faulty merging of photometry from different filters. Of the 33 sources in the ‘conservative’ box in Figure 11, all are also detected at $5.8 \mu\text{m}$ and all but one are detected at $8.0 \mu\text{m}$. Additionally, the SEDs of these objects show no unexpected features, such as those that would be obvious if the flux in one filter from a red giant was merged with the other three filters from an AGB star. Some caution is in order here, however, because the total mass-loss in WLM is dominated by only a few sources and the super-wind phase of mass-loss for an individual AGB star is very short ($\sim 5 \times 10^4$ years; Vassiliadis & Wood 1993) compared to evolutionary timescale for the entire stellar population. Consequently, the mass-loss measured at the present epoch may not be representative of the average mass-loss over an extended period in the galaxy.

We compare these mass-loss values with the models from Kennicutt et al. (1994) which estimate the return of material into the ISM from a single-age stellar population. They find 26-46% of the initial stellar mass is returned into the ISM via supernovae and AGB winds, depending on the assumed IMF, and show most of this material is returned within the first Gyr. Dolphin et al. (2005) finds the star formation rate over the last Gyr in one HST/WFPC2 field in WLM to be $1 \times 10^{-3} M_{\odot} \text{ yr}^{-1}$. Within this WFPC2 field we detect seven AGBs in the IR that contribute a total MLR of $1.8-3.8 \times 10^{-4} M_{\odot} \text{ yr}^{-1}$. Consequently,

our conservative MLR represents a 18-38% return of mass into the ISM. van Loon et al. (2005) showed that about half of the total mass-loss an AGB star experiences occurs in the dust-enshrouded phase. Because the AGBs we use to calculate this rate all have red [3.6]–[4.5] colors that are indicative of the dust-enshrouded phase, to estimate the total mass-loss from these objects it is reasonable to adjust this value upward by a factor of two, to 36-76%. These values are probably overestimated, given that they are higher than the Kennicutt et al. (1994) prediction and we are not measuring the contribution of material from supernovae and massive AGBs that have already died. Some possible explanations for this overestimation are the lower limit for our assumed dust-to-gas ratio may be too low, which would increase the derived MLR for a given wind optical depth, and also any ‘burstiness’ in the true star formation rate, which could either raise or lower the calculated fraction being returned to the ISM compared to the average value over the past Gyr. Given the fluctuations observed in the star formation histories of dIs, the factor of two agreement is probably quite reasonable.

In Figure 12 we show a histogram of the fraction of objects brighter than the TRGB that were detected in the optical as a function of [3.6]–[4.5] color (left panel) and optical depth for carbon-rich AGBs with 85% AMC and 15% SiC wind and two different effective temperatures (right panel). This figure clearly shows the trend of decreasing optical completeness with increasing MLR, which supports our conclusion that the AGB stars misidentified or not detected in the optical have been reddened by circumstellar material.

Frost et al. (1998) report that there are very few optically detected carbon stars in the Large Magellanic Cloud (LMC) with MLRs above $10^{-6} M_{\odot} \text{ yr}^{-1}$, and none above $10^{-5} M_{\odot} \text{ yr}^{-1}$. They adopt a value of $\dot{M} = 5 \times 10^{-6} M_{\odot} \text{ yr}^{-1}$ as the critical value above which no carbon star will be detected optically. We detect no AGBs optically with $[3.6]–[4.5] > 1.0$ ($\tau = 1.3$, $\dot{M} \sim 5 \times 10^{-5} M_{\odot} \text{ yr}^{-1}$ assuming $L = 3000 L_{\odot}$) and only one with $[3.6]–[4.5] > 0.85$ ($\tau = 0.7$, $\dot{M} \sim 2 \times 10^{-5} M_{\odot} \text{ yr}^{-1}$) out of the 14 AGBs detected in the IR. Given the difference in metallicity of the LMC and WLM (~ 0.7 dex) and its effect on the derived MLR, these values are in agreement with the Frost et al. (1998) result.

Figure 13 shows the MLR versus bolometric luminosity for all of the objects brighter than the TRGB in our IR CMD. Filled circles represent the MLRs and luminosities assuming all of the AGBs are carbon-rich with dust-to-gas ratios of 7.9×10^{-4} , winds composed of 85% AMC and 15% SiC, and $T_{eff} = 2650$ K. Open circles are for the same composition with $T_{eff} = 3600$ K. We also show the classical single-scattering mass-loss limit (bottom dashed line) and the empirical maximum mass-loss limit found for the LMC (top solid line) as plotted in van Loon et al. (1999). Because we do not know the effective stellar temperature a priori, some MLRs can be overestimated in the case of the $T_{eff} = 3600$ K template or

underestimated for $T_{eff} = 2650$ K, since there is a degeneracy in our CMDs between stars with cool effective temperatures and stars with warmer effective temperatures but significant MLRs. Consequently, some caution should be taken in strictly interpreting this plot. The dust-to-gas ratio assumed for this plot is the upper limit of the two values we consider in this paper. By instead assuming the lower limit, all mass-loss rates would be scaled upward by approximately a factor of two.

Despite these uncertainties, there is a remarkable consistency between the AGB populations of WLM and both the LMC and SMC van Loon et al. (1999, 2006b). Under the assumption of $T_{eff} = 2650$ K, the empirical maximum MLR found in the LMC by van Loon et al. (1999) is in excellent agreement with the AGBs in WLM. We also detect many AGBs that are consistent with $\dot{M} = 10^{-7} M_{\odot} \text{ yr}^{-1}$ and $M_{bol} = -4$. AGBs with these properties were also seen in the LMC van Loon et al. (1999), though relatively few due to sensitivity considerations. Gail & Sedlmayr (1987) show that these objects could not exist if the wind-driving mechanism was purely by the classical method of radiation pressure accelerating dust grains whose momenta are coupled to circumstellar gas (Gehrz & Woolf 1971). These observations support those of van Loon et al. (1999), suggesting another mechanism may be at work.

5.4. Luminosity Contribution From AGB Stars

One of the reasons for observing galaxies in the IR is to obtain accurate measurements of their stellar masses. When using luminosity measurements to estimate stellar masses at any wavelength, it is important to understand the stellar types contributing to that luminosity. In the optical, the luminosity can be dominated by massive, young stars that describe only the very recent star formation rate, while in the near-IR the luminosity is from old red giants (in the short-wavelength near-IR) or intermediate age AGB stars (in the IRAC bands). Nearby galaxies offer us the opportunity to determine precisely which stars contribute to a galaxy’s total luminosity as a function of wavelength. As we note in §5, for the point sources detected at 3.6 and 4.5 μm , 79% of the total flux is from AGB stars, in contrast with optical and shorter wavelength near-IR studies.

Lee et al. (2006) used 4.5 μm luminosities to estimate total stellar masses of nearby dwarf galaxies. We recover 83% of the total 4.5 μm flux Lee et al. (2006) find for WLM in point sources we detect at both 3.6 and 4.5 μm . Although the 4.5 μm luminosity of WLM is dominated by the light from AGB stars, because the evolutionary phase of AGB star production is relatively long, the 4.5 μm luminosity is a fairly robust measure of the stellar mass (i.e., short-term variations in the SFH are averaged out). However, for smaller galaxies

or galaxies with unusual SFHs, the $4.5 \mu\text{m}$ luminosity may be less directly connected to the stellar mass.

van Loon et al. (2005) provided a method of estimating the masses of stellar clusters based on the number of stars brighter than the TRGB in the L' band ($3.76 \mu\text{m}$) and the age of the cluster. Performing this calculation for WLM is somewhat difficult because, unlike stellar clusters, its stellar population is not single aged. However, by adopting an age of 2 Gyr for the stellar population (i.e., the age of the recent star forming event that formed a significant fraction of the stars; Dolphin 2000), we arrive at a total stellar mass of $1.1 \times 10^7 M_\odot$. Because of the range in age of the stellar population and our incomplete sky coverage this value is probably uncertain by at least 50%; however, it is reasonably consistent with the Lee et al. (2006) value of $1.8 \times 10^7 M_\odot$.

6. Results and Conclusions

We have presented *Spitzer*/IRAC imaging at 3.6 and $4.5 \mu\text{m}$. V and I optical data from the LGGS (Massey et al. 2006) were combined with these observations to help determine the stellar types of objects detected in the IR. We find that above the TRGB at $3.6 \mu\text{m}$, 39% of the objects were undetected in the optical and 43% were undetected or misidentified, even though the Massey et al. (2006) data are 50% complete 3 magnitudes below the TRGB. It is likely that many of these objects were not detected in the optical due to dust production in the winds of the AGB stars, which efficiently absorb visible photons while IR radiation is relatively unaffected.

Comparing our photometry with the narrow-band optical study of WLM (Battinelli & Demers 2004), we detect nearly all of the objects they classify as carbon stars with a few exceptions, mostly due to crowding effects. However, of the 691 stars we detect and classify as AGBs only 18% were detected by the narrow-band study. It is unclear what effect this may have on the assumed C/M ratio, since there is evidence that both mass-losing carbon stars and M-type AGBs both escaped detection in the Battinelli & Demers (2004) study.

Additionally, we detect a significant population of objects with positions on the IR CMD consistent with mass-losing AGBs. For these objects we derive a conservative total MLR for the galaxy of $0.7\text{--}1.6 \times 10^{-3} M_\odot \text{ yr}^{-1}$, assuming the entire population is composed of carbon stars. If we include all of our 3.6 and $4.5 \mu\text{m}$ detections, we find a total MLR of up to $0.9\text{--}2.4 \times 10^{-3} M_\odot \text{ yr}^{-1}$, which is likely an overestimate due to the inclusion of objects photometrically scattered to their relatively red positions in the IR CMD.

For the region of the galaxy covered by the HST/WFPC2 study of Dolphin (2000), we

find 36-76% of the initial mass in stars formed over the last Gyr is currently being returned into the ISM via mass-loss from AGB stars, assuming half of the total mass lost by an AGB star occurs in the dust enshrouded phase. This value is somewhat higher than expected, given a total of 26-46% is estimated to be returned from the entire stellar population (Kennicutt et al. 1994), and our data are not sensitive to the contribution from supernovae and AGBs that have already died. The prescription we use may systematically overestimate the MLRs.

We find the distribution of MLRs and bolometric luminosities of AGBs and RSGs are very similar to those in the LMC and SMC (van Loon et al. 1999, 2006b) and the empirically derived maximum MLR of the LMC (van Loon et al. 1999) is in excellent agreement with our data.

Finally, we show that the AGB stars, which trace the intermediate age stellar population, provide the dominant contribution to the luminosity in the IRAC bands, while studies at shorter wavelengths can preferentially detect either much younger sources (in the optical) or older age populations (short-wavelength near-IR).

We thank Martin Groenewegen for his comments on a previous version of this manuscript and for providing his models of mass-losing AGBs prior to publication. We thank Jacco van Loon and Maria-Rosa Cioni for their valuable comments and suggestions, which contributed significantly to the presentation of these data. We also thank the anonymous referee for their prompt and careful reading of the manuscript and their valuable comments. E. D. S. acknowledges partial support from a NASA LTSARP grant NAG 5-9221 and the University of Minnesota. This work is based in part on observations made with the Spitzer Space Telescope, which is operated by the Jet Propulsion Laboratory, California Institute of Technology under NASA contract 1407. Support for this work was provided by NASA through Contract Numbers 1256406 and 1215746 issued by JPL/Caltech to the University of Minnesota. This research has made use of NASA’s Astrophysics Data System Bibliographic Services and the NASA/IPAC Extragalactic Database (NED) which is operated by the Jet Propulsion Laboratory, California Institute of Technology, under contract with the National Aeronautics and Space Administration.

REFERENCES

Ables, H. D. & Ables, P. G. 1977, *ApJ*, 34, 245
Albert, L., Demers, S., & Kunkel, W. E. 2000, *AJ*, 119, 2780

Babusiaux, C., Gilmore, G., & Irwin, M. 2005, MNRAS, 359, 985

Battinelli, P., Demers, S., & Letarte, B. 2003, AJ, 125, 1298

Battinelli, P., & Demers, S. 2004, A&A, 416, 111

Battinelli, P., & Demers, S. 2005, A&A, 434, 657

Boyer, M. L., Woodward, C. E., van Loon, J. Th., Gordon, K. D., Evans, A., Gehrz, R. D., Helton, L. A., Polomski, E. F. 2006

Bresolin, F., Pietrzynski, G., Urbaneja, M. A., Gieren, W., Kudritzki, R. P., & Venn, K. A. 2006, ApJ, in press, astro-ph/0605640

Cioni, M.-R. L., & Habing, H. J. 2005, A&A, 429, 837

Cook, K. H., Aaronson, M., & Norris, J. 1986 ApJ, 305, 634

Davidge, T. J. 2005, AJ, 130, 2087

Dolphin, A.E., 2000, ApJ, 531, 804

Dolphin, A. E. 2002, MNRAS, 332, 91

Dolphin, A.E., Weisz, D. R., Skillman, E. D., Holtzman, J.A. 2005, ASP Conf. Ser., in press, astro-ph/0506430

Fazio, G. G., et al. 2004, ApJS, 154, 10

Frost, C. A., Cannon, R. C., Lattanzio, J. C., Wood, P. R., & Forestini, M. 1998, A&A, 332, L17

Gail, H.-P., & Sedlmayr, E. 1987, A&A, 177, 186

Gallouet, L., Heidmann, N., & Dampierre, F. 1975, A&AS, 19, 1

Gehrz, R. D., & Woolf, N. J. 1971, ApJ, 165, 285

Groenewegen, M. A. T. 2006, A&A, 448, 181

Hodge, P., & Miller, B. W. 1995, ApJ, 451, 176

Hodge, P. W., Dolphin, A. E., Smith, T. R., & Mateo, M. 1999, ApJ, 521, 577

Holtzman, J., Afonso, C., & Dolphin, A. 2003, ApJ, accepted

Huchtmeier, W. K., Seiradakis, J. H., & Materne, J. 1981, A&A, 102, 134

Huchtmeier, W. K., & Richter, O. G. 1986, A&AS, 63, 323

Hunter, D. A., Hawley, W. N., & Gallagher, J. S. 1993, AJ, 106, 5

Iben, I., & Renzini, A. 1983, ARA&A, 21, 271

Indebetouw, R. et al. 2005, ApJ, 619, 931

Jackson, D. C., Skillman, E. D., Cannon, J. M., & Côté, S. 2004, AJ, 128, 1219

Jackson, D. C., Cannon, J. M., Skillman, E. D., Lee, H., Gehrzi, R. D., Woodward, C. E., & Polomski, E. 2006, ApJ, 646, 192

Jones, T. J., Woodward, C. E., Boyer, M. L., Gehrzi, R. D., & Polomski, E. 2005, ApJ, 620, 731

Jura, M. 1984, ApJ, 282, 200

Kang, A., Sohn, Y.-J., Rhee, J., Shin, M., Chun, M.-S., & Kim, H.-I. 2005, A&A, 437, 61

Kennicutt, R. C., Tamblyn, P., & Congdon, C. E. 1994, ApJ, 435, 22

Lee, H., Skillman, E. D., & Venn, K. A. 2005, ApJ, 620, 223

Lee, H., Skillman, E. D., Cannon, J. M., Jackson, D. C., Gehrzi, R. D., Polomski, E., & Woodward, C. E. 2006, ApJ, accepted

Letarte, B., Demers, S., Battinelli, P., & Kunkel, W. E. 2002, AJ, 123, 832

Massey, P., Olsen, K. A. G., Hodge, P. W., Strong, S. B., Jacoby, G. H., Schlingman, W., & Smith, R. C. 2006, AJ, 131, 2478

Mateo, M. L. 1998, ARA&A, 36, 435

Melotte, P. J. 1926 MNRAS, 86, 636

Minniti, D., & Zijlstra, A. A. 1997, AJ, 114, 147

Nowotny, W., Kerschbaum, F., Schwarz, H. E., & Olofsson, H. 2001, A&A, 367, 557

Reach, W. T., et al. 2005, PASP, 117, 978

Rejkuba, M., Minniti, D., Gregg, M. D., Zijlstra, A. A., Alonso, M. V., & Goudfrooij, P. 2000, AJ, 120, 801

Rieke, G. H., & Lebofsky, M. J. 1985, *ApJ*, 288, 618

Robin, A. C., Reylé, C., Derrière, S., & Picaud, S. 2003, *A&A*, 409, 523

Skillman, E. D., Terlevich, R., & Melnick, J. 1989, *MNRAS*, 240, 563

Sohn, Y.-J., Kang, A., Rhee, J., Shin, M., Chun, M.-S., & Kim, H.-I. 2006, *A&A*, 445, 69

Stetson, P.B. 1987, *PASP*, 99, 191

van den Bergh, S. 1994, *AJ*, 107, 1328

van den Bergh, S. 2000, *The Galaxies of the Local Group 2000*, Vol. 35 (Cambridge, UK: Cambridge University Press)

van Loon, J. T., Zijlstra, A. A., Whitelock, P. A., Waters, L. B. F. M., Loup, C., & Trams, N. R. 1997, *A&A*, 325, 585

van Loon, J. T., Zijlstra, A. A., & Groenewegen, M. A. T. 1999, *A&A*, 346, 805

van Loon, J. T., Marshall, J. R., & Zijlstra, A. A. 2005, *A&A*, 442, 597

van Loon, J. T., Marshall, J. R., Cohen, M., Matsuura, M., Wood, P. R., Yamamura, I., & Zijlstra, A. A. 2006, *A&A*, 447, 971

van Loon, J. T. 2006, *ASP Conf. Ser.*, in press, astro-ph/0512326

Vassiliadis, E., & Wood, P. R. 1993, *ApJ*, 413, 641

Wallerstein, G., & Knapp, G. R. 1998, *ARA&A*, 36, 369

Werner, M. W., et al. 2004, *ApJS*, 154, 1

Wolf, M. 1909, *Astron. Nachr.*, 183, 187

Wood, P. R., Bessell, M. S., & Fox, M. W. 1983, *ApJ*, 272, 99

Wood, P. 1998, *A&A*, 338, 592

Zijlstra, A. A., Loup, C., Waters, L. B. F. M., Whitelock, P. A., van Loon, J. T., & Guglielmo, F. 1996, *MNRAS*, 279, 32

Table 1. Basic Properties of WLM

Quantity	Value	Reference
Right Ascension, α (2000)	00 01 57.8	1
Declination, δ (2000)	-15 27 51	1
Heliocentric velocity, V_\odot (km s $^{-1}$)	-130 km s $^{-1}$	5
Distance, D (Mpc)	0.92 ± 0.04	6
Morphological Type	Ir IV-V	4
12 + log(O/H)	7.83	6
Total H I mass (M $_\odot$)	5.3×10^7	3
Inclination angle (degrees)	69	2
Position angle (degrees)	181	5
Rotational velocity (km s $^{-1}$)	38	5
Conversion factor (pc/arcmin)	276	5

References. — (1) Gallouet et al. (1975). (2) Ables & Ables (1977). (3) Huchtmeier et al. (1981). (4) van den Bergh (1994). (5) Jackson et al. (2004). (6) Lee et al. (2006).

Table 2. Detection Statistics

Total Point Source Detections in All Wavelengths	
Filter	Number
Both V and I	4989
3.6 μ m	2855
4.5 μ m	2019
5.8 μ m	300
8.0 μ m	122
Detections in All Four IRAC bands, But Not V and I	
Object type	Number
Total	46
RSG (Above the AGB limit)	5
AGB/RSG (Above the TRGB, below the AGB limit)	41
3.6 μ m Point Source Flux (Total Flux = 46.5 mJy)	
Object type	Fraction
Brighter than the TRGB	79%
Fainter than the TRGB	21%
Optical Detection Fractions of IR Identified AGBs	
Filter	Fraction
V and I	61%
Detected but misidentified in V and I	4%
Narrow-band optical	16%

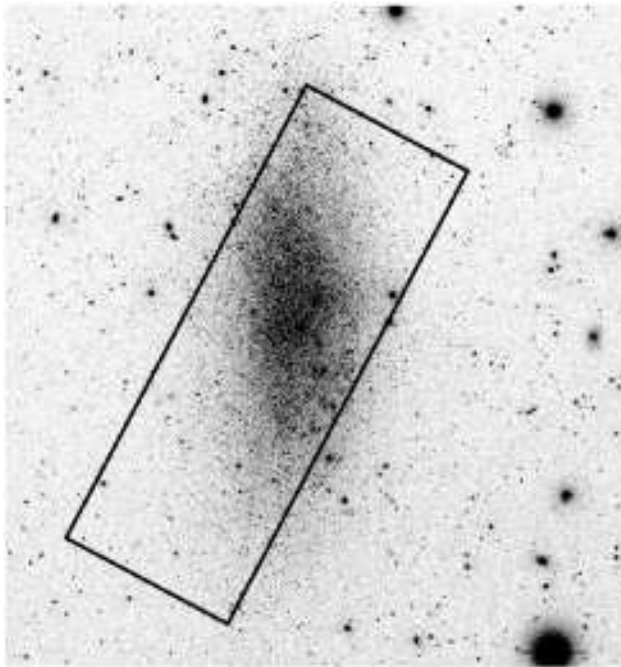


Fig. 1.— LGGS I-band image of WLM from Massey et al. (2006). The region with coverage in all four IRAC bands is overlayed in black. North is up and East is left.

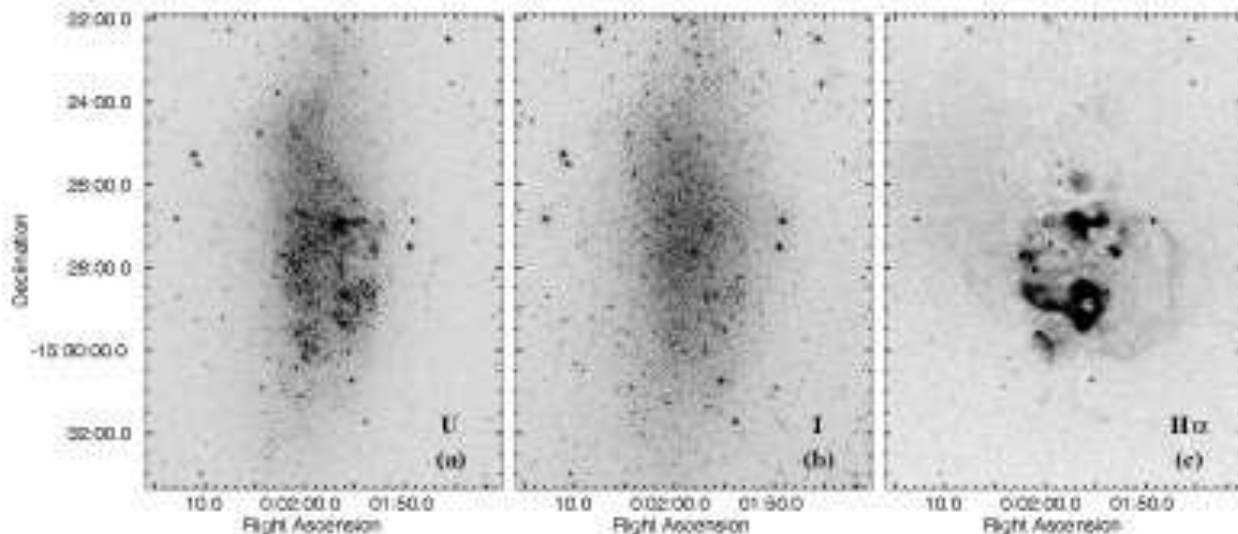


Fig. 2.— (a) U, (b) I, and (c) continuum subtracted H α images of WLM from the LGGS (Massey et al. 2006), showing the change in morphology with wavelength. Note the concentration of recent star formation in the south.

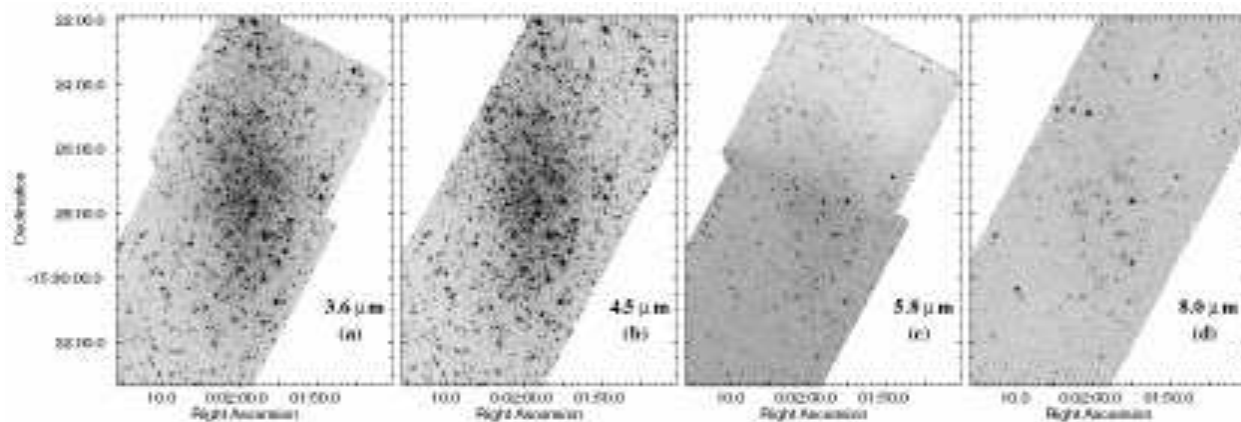


Fig. 3.— IRAC 3.6 μm (a), 4.5 μm (b), 5.8 μm (c), and 8.0 μm (d) images of WLM. Due to both decreased sensitivity and fainter stellar emission at longer wavelengths we detect significantly few objects than in the short wavelength bands.

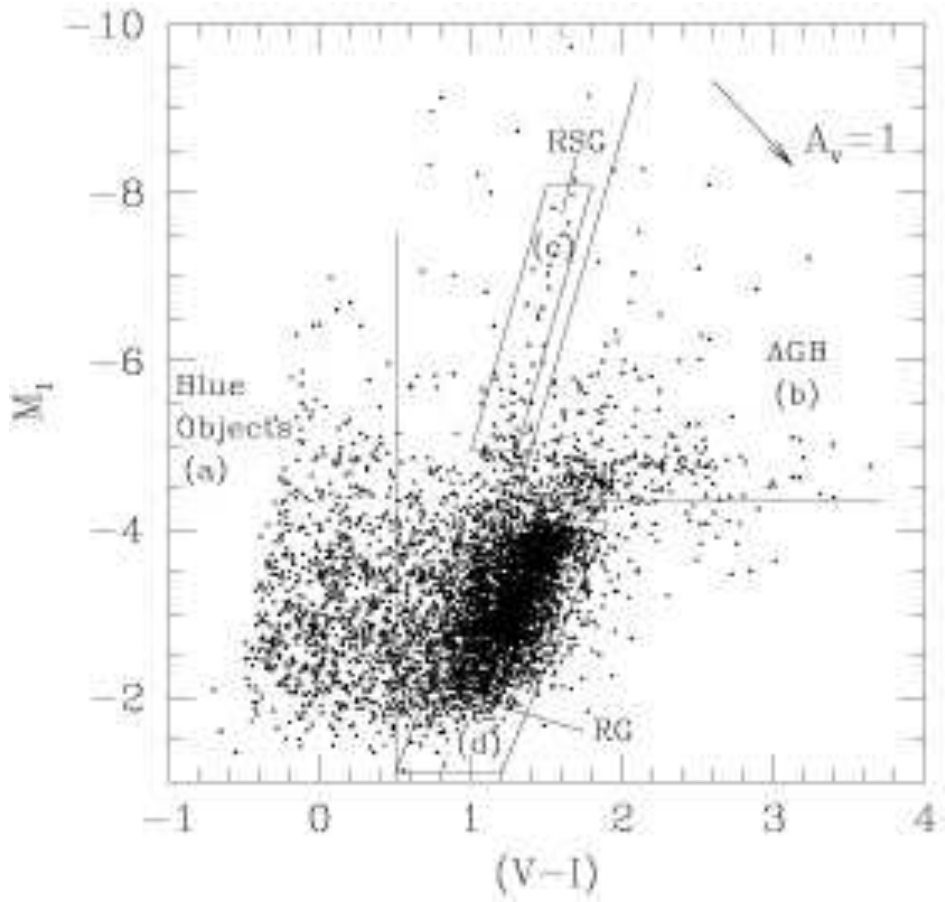


Fig. 4.— Absolute I versus V–I CMD from the optical data. Regions consisting of blue objects (a; left of the vertical line at $V-I = 0.5$), AGB stars (b), red supergiants (c), and red giants (d) refer to the the IRAC detections displayed in Figure 5.

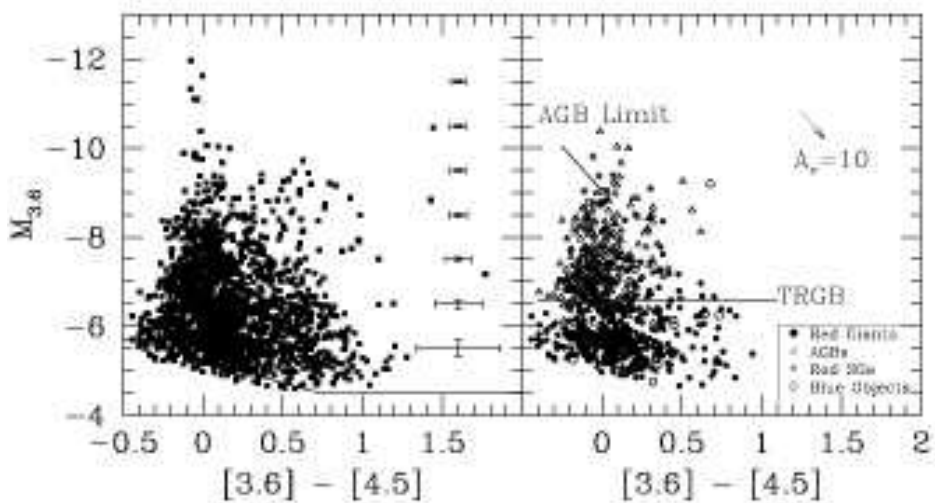


Fig. 5.— IRAC absolute $3.6 \mu\text{m}$ versus $[3.6] - [4.5]$ color-magnitude diagrams for all of the *Spitzer* data (left) and separated by optical classification for the objects detected in both the optical and IR (right; see Figure 4). The left panel shows $1-\sigma$ error bars averaged over each magnitude bin and the 50% completeness limit (see §4 for details). The right panel shows a line connecting the AGB limits for a G0 and M5 stars, a reddening vector for 10 magnitudes of visual extinction, and the red giant branch tip. Note the paucity of optically detected stars with very red IR colors.

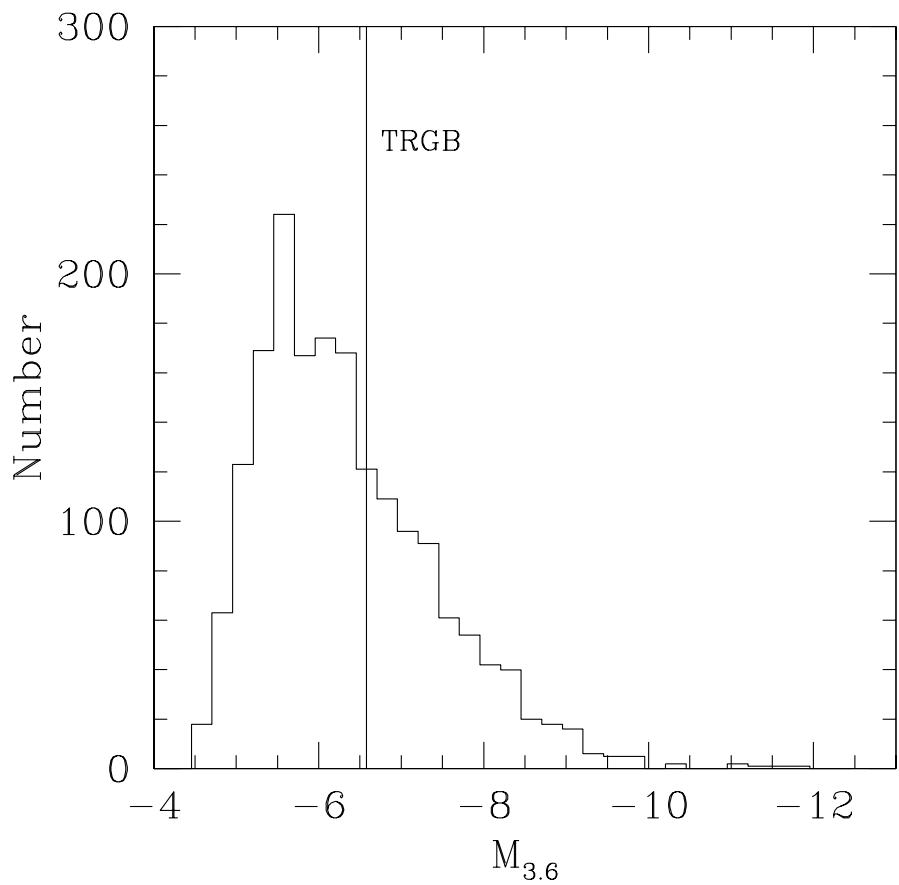


Fig. 6.— The 3.6 μ m luminosity distribution (number of stars per 0.25 magnitude bin) for stars detected at both 3.6 and 4.5 μ m. The TRGB is labeled at $M_{3.6} = -6.6$.

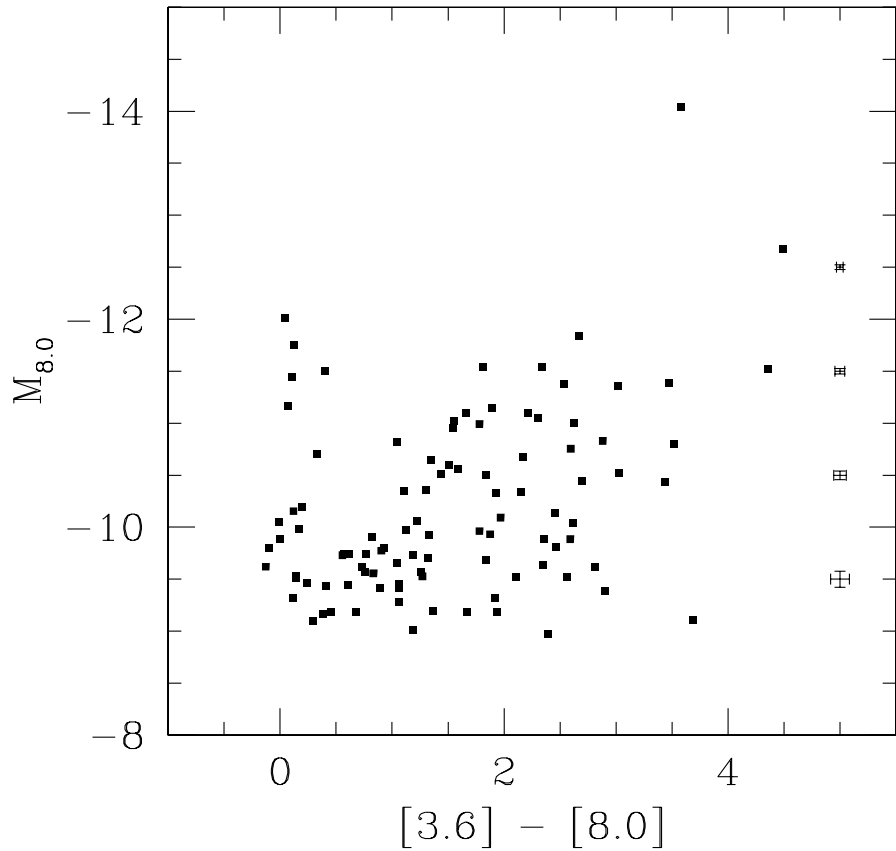


Fig. 7.— IRAC absolute $3.6 \mu\text{m}$ versus $[3.6] - [8.0]$ color-magnitude diagram. We observe two separate populations; a narrow distribution with $-12 < M_{3.6} < -9$ and $[3.6] - [8.0] \sim 0$ and another, much broader, distribution with $-12 < M_{3.6} < -9$ and $1 < [3.6] - [8.0] < 4$ that are likely AGBs losing significant mass. Representative 1- σ errorbars are shown at right.

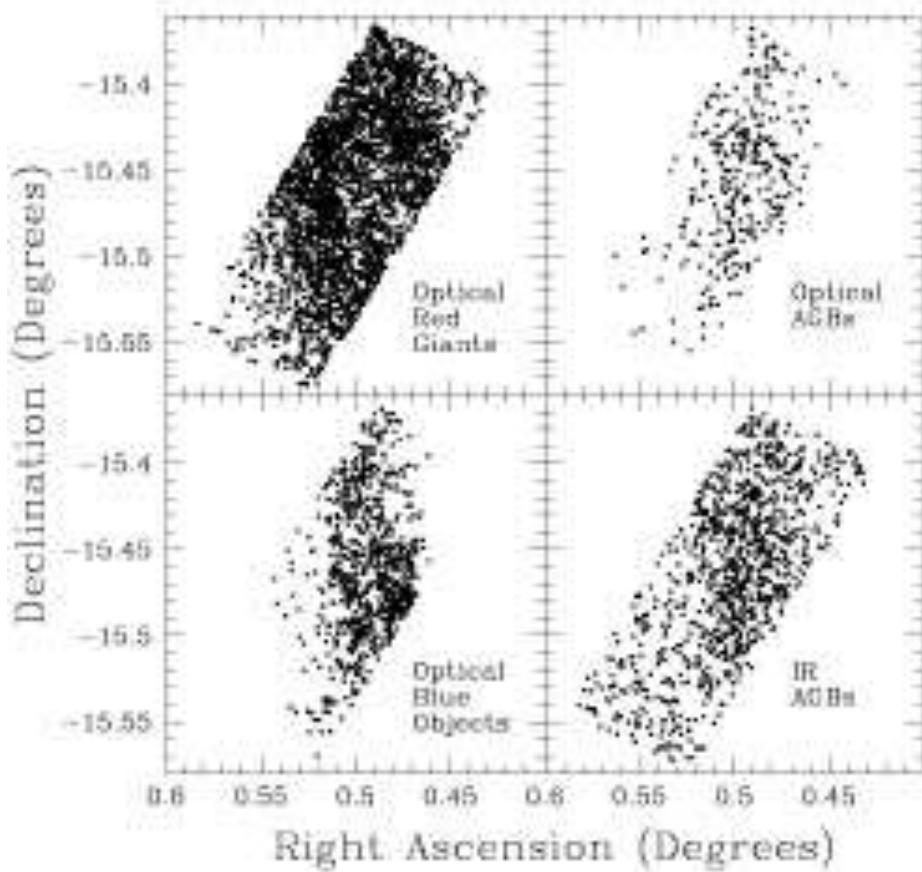


Fig. 8.— Positions of stars as classified in the optical (see Figure 4), except for the bottom right panel, which shows the positions of AGB stars detected in the IR.

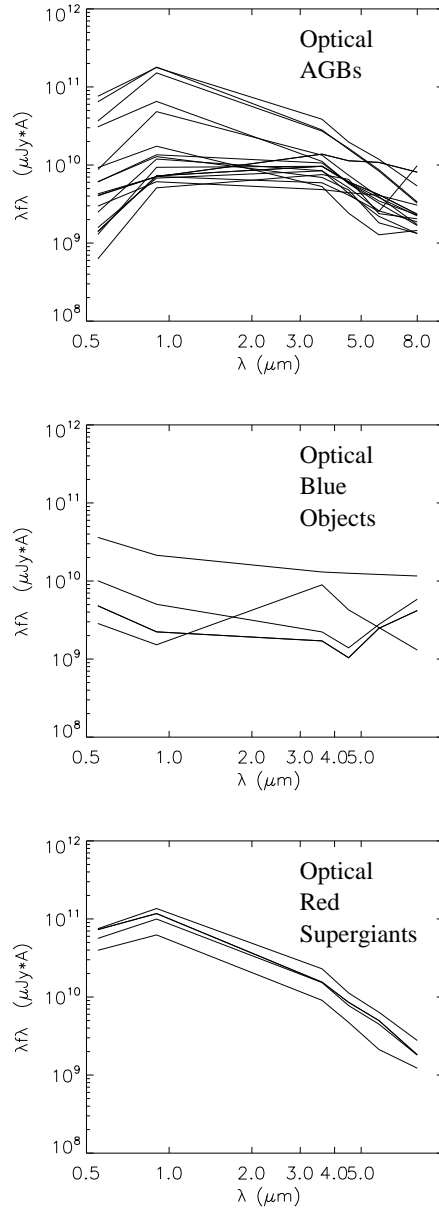


Fig. 9.— LGGS V and I and IRAC 3-8 μm spectral energy distributions of (top to bottom) optically identified AGB stars, blue objects, and red supergiants. Note, in particular, the similarities between the AGB stars and the RSGs.

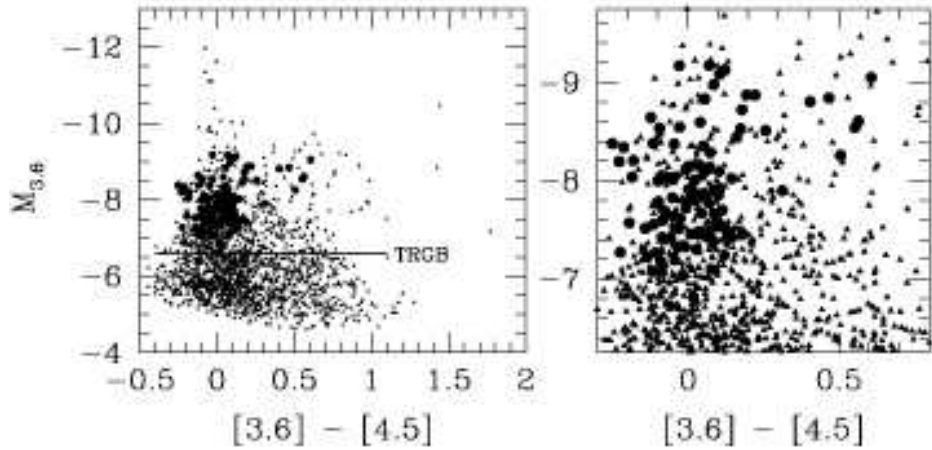


Fig. 10.— IRAC absolute $3.6 \mu\text{m}$ versus $[3.6] - [4.5]$ color-magnitude diagram. The small triangles are our IRAC photometry and the large circles are our measurements of the carbon stars identified by Battinelli & Demers (2004). The right panel is a blow-up of the left panel to more easily distinguish the points.

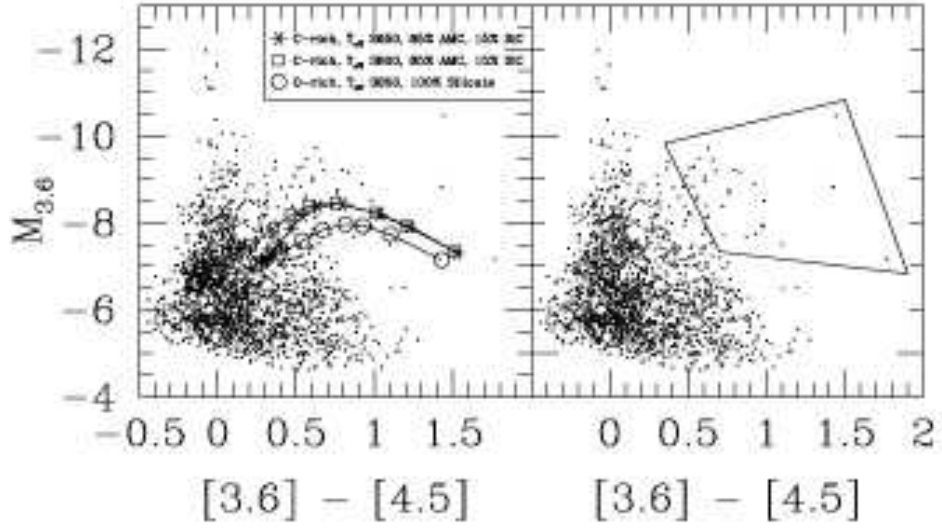


Fig. 11.— IRAC absolute $3.6 \mu\text{m}$ versus $[3.6] - [4.5]$ color-magnitude diagrams. The left panel shows tracks for mass-losing AGBs with luminosity of $3000 L_\odot$, expansion velocity of 10 km s^{-1} , dust-to-gas ratio of 7.9×10^{-4} , and three different compositions and increasing (from left to right) mass-loss rates from 6×10^{-10} to 6×10^{-5} for the carbon-rich tracks and from 6×10^{-10} to $1 \times 10^{-4} M_\odot \text{ yr}^{-1}$ for the oxygen-rich track. The box on the right panel shows the objects selected to derive the conservative total mass-loss rate discussed in §5.3.

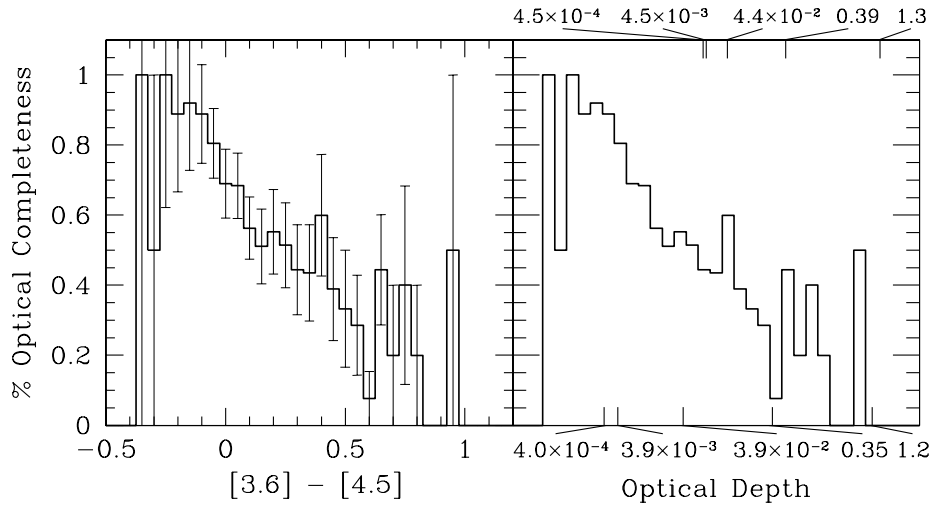


Fig. 12.— The fraction of objects brighter than the TRGB at $3.6 \mu\text{m}$ that are detected in the optical as a function of $[3.6]-[4.5]$ color (left panel) and wind optical depth (right panel) for a carbon-rich AGB with 85% AMC and 15% SiC wind and effective temperatures of 2650 K (top axis) and 3600 K (bottom axis). The errorbars were determined by taking the square root of the number of optically detected objects divided by the total number detected at 3.6 and $4.5 \mu\text{m}$. The trend of decreasing optical completeness with increasing optical depth (and MLR) is clearly shown.

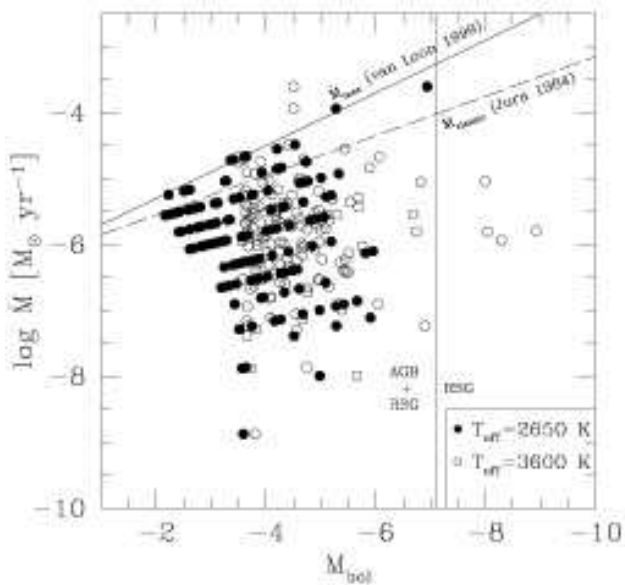


Fig. 13.— Mass-loss rates versus bolometric magnitude for all objects brighter than the TRGB at $3.6 \mu\text{m}$, assuming dust-to-gas ratio of 7.9×10^{-4} , a wind composition of 85% AMC + 15% SiC and effective temperatures of $T_{\text{eff}} = 2650$ (filled circles) and $T_{\text{eff}} = 3600$ (open circles), following van Loon et al. (1999). The bottom dashed line is the classical single-scattering mass-loss limit (Jura 1984) and the top solid line is the empirical maximum mass-loss limit suggested for the LMC by van Loon et al. (1999). The AGB limit is shown (vertical line) at $M_{\text{bol}} = -7.1$. See §5.3 for discussion.